Monthly Notices of the ROYAL ASTRONOMICAL SOCIETY

MNRAS **533,** 3999–4006 (2024) https://doi.org/10.1093/mnras/stae2032
Advance Access publication 2024 September 2

Atmospheric ion escape and solar wind deposition as a function of planetary radius

P. C. Hinton [1,2,3★] D. A. Brain [1,2] N. R. Schnepf [2] R. Jarvinen [4] and R. Ramstad [2]

[1] *Department of Astrophysical and Planetary Sciences, University of Colorado, Boulder, CO 80309, USA*
[2] *Laboratory for Atmosphere and Space Physics, Boulder, CO 80303, USA*
[3] *National Solar Observatory, Boulder, CO 80303, USA*
[4] *Finnish Meteorological Institute, FI-00101 Helsinki, Finland*

Accepted 2024 August 22. Received 2024 July 29; in original form 2024 June 14

ABSTRACT

We explore the ability of an unmagnetized planet to retain an atmosphere as a function of its radius. We use a particle-in-cell hybrid code to simulate the global plasma interaction of unmagnetized terrestrial planets at 1 au under average solar wind conditions. We vary the radius of the planet (R_p) from Mars-sized (3390 km) to super-Earth-sized (9390 km). We inject hydrogen and oxygen ion outflows from the ionosphere and quantify how the ion escape, recirculation, solar wind deposition, and net atmospheric mass flux vary as a function of planetary radius. We find that as the radius and the corresponding ionospheric outflow rate are varied, the fraction of outflowing H^+ that escapes remains at 15.5 ± 1.0 per cent, while the rest recirculates back towards the planet. The fraction of produced O^+ that escapes from a Mars-sized planet is 27 ± 1 per cent, and decreases to 7 ± 1 per cent for super-Earth, suggesting that smaller planets are less able to retain heavy ions. We find, however, that larger planets have lower solar wind deposition fractions because their bow shocks are at greater distances from the surface of the planet. The ionospheric outflow rate at which mass deposition is equal to mass escape is found to be proportional to R_p^2. Lastly, we propose that the bulk gyration of the solar wind at the induced magnetosphere can lead to differential escape trajectories of light and heavy ions.

Key words: (Sun:) solar–terrestrial relations – planets and satellites: atmospheres – planets and satellites: magnetic fields.

1 INTRODUCTION

Geological evidence on Mars suggests that the red planet once hosted a dense atmosphere that supported the existence of surface oceans (e.g. Carr & Waenke 1992; di Achille & Hynek 2010). However, as time has passed, much of the Martian atmosphere appears to have escaped to space (e.g. Lillis et al. 2015). Some argue that when the Martian dynamo ended and the global intrinsic magnetic field subsequently disappeared, the planet's atmosphere became exposed to the solar wind and was stripped away (e.g. Jakosky 2022). If the Earth's geodynamo were to shut off, could it be susceptible to atmospheric solar wind ablation? This raises the broader question of whether planets are able to host habitable atmospheres without intrinsic magnetic fields. These are not simple questions to answer due to the plethora of variables that influence atmospheric escape. In this study, we analyse the role of one variable, the planetary radius (R_p), in an attempt to begin constraining the possible answers to these questions.

Atmospheric escape can be broken into two categories: the escape of neutral atoms and the escape of ions (e.g. Brain et al. 2016). In this study, we focus on the escape of ions, most of which are produced at or near the sub-solar point of the planet via photoionization and subsequent electron impact ionization (Haider, Mahajan & Kallio 2011; Richards & Voglozin 2011). As the radius of the planet is increased, the mass (M_p) also increases (e.g. Valencia, O'Connell & Sasselov 2006), as does the escape velocity (v_{esc}). Numerous previous studies have assumed v_{esc} to be a controlling parameter for ion escape (e.g. Ergun et al. 2006; Dubinin et al. 2009). A recent study, which also analysed ion escape as a function of R_p, found that escape generally decreased as R_p increased, and suggested that these changes were potentially caused by increased v_{esc} (Chin, Dong & Lingam 2024).

However, test particle analysis has indicated that non-thermal escape is primarily controlled by electromagnetic forces, not by the gravitational force (Fang et al. 2008, 2010). A quick comparison of these forces for demagnetized Earth explains these findings. The force of gravity (F_g) on a proton in the ionosphere of Earth ($R_E + 300$ km) has a magnitude of 1.5×10^{-26} N, whereas the solar wind convection electric field has a typical strength of 1–3 mV m^{-1} in Earth's rest frame (e.g. Slavin & Holzer 1981) and global hybrid models predict 0.1–1 mV m^{-1} fields in induced magnetospheres (Wang et al. 2023). These yield electric forces ($\boldsymbol{F}_E = q\boldsymbol{E}_{sw}$) that are three to four orders of magnitude stronger than the force of gravity.

Spacecraft observations at Mars find that O^+ escapes in the $+E_{sw}$ hemisphere in the form of a large heavy ion plume (Dong et al. 2015). Additionally, test particle analysis finds that the location of the ion production strongly influences whether it will escape in the plume or recirculate back to the planet (Fang et al. 2010). Kinetic

★ E-mail: pahi9557@colorado.edu

recirculation occurs when planetary ions are accelerated in the solar wind interaction and directed back towards the ionosphere. Kinetic recirculation and the Martian heavy ion plume are well modelled by Jarvinen et al. (2018), who use a particle-in-cell code called RHYBRID to track the trajectory of macro-ions.

The plume's morphology is explained by the oxygen ion's large gyroradius combined with $\boldsymbol{E} \times \boldsymbol{B}$ drift motion (Jarvinen et al. 2010; Jarvinen, Brain & Luhmann 2016). Models that do not include ion-kinetic effects (e.g. Sun et al. 2023; Chin et al. 2024) will not be able to reproduce the heavy ion plume (Egan et al. 2018). The same physical mechanisms that result in the Martian plume should continue to operate as the planetary radius is increased; this explains the evidence for an analogous heavy ion plume on Venus (Xu et al. 2023). In order to include the heavy ion plume and possible kinetic recirculation effects at each planet, we have chosen to use RHYBRID in this study. We report changes in plume morphology as R_p is increased.

We start with a Mars-sized planet ($R_\mathrm{p} = 3390$ km) at 1 au, and use RHYBRID to model the interaction of planetary ionospheric outflows with the solar wind. This allows us to observe the escape paths of different ion species and quantify what percentage of the outflow escapes versus what percentage recirculates back towards each planet. We then incrementally increase the radius of the planet by 2000 km up to $R_\mathrm{p} = 9390$ km. We include a planet with $R_\mathrm{p} = 6371$ km, which is the Earth's radius. The deposition rate of solar wind protons on to each planet is calculated. Combining the deposition rates with the escape rates yields the net mass flux of each simulation's atmosphere. Lastly, we find that the ionospheric outflow rate at which the atmosphere's net mass flux is equal to zero is proportional to R_p^2.

2 METHODS

2.1 RHYBRID

RHYBRID is a particle-in-cell code that utilizes ion macroparticles and treats electrons as a charge-neutralizing fluid (Jarvinen et al. 2018). Ions are macroscopic particle clouds (macroparticles) propagated via the Lorentz force

$$m_i \frac{\mathrm{d}\boldsymbol{v}_i}{\mathrm{d}t} = q_i(\boldsymbol{E} + \boldsymbol{v}_i \times \boldsymbol{B}), \tag{1}$$

where i is the ion in question, m is the mass, q is the electric charge, and v is the velocity. The magnetic field (B) is propagated via Faraday's law

$$\frac{\partial \boldsymbol{B}}{\partial t} = -\nabla \times \boldsymbol{E}, \tag{2}$$

which leads to self-consistent generation of an induced planetary magnetosphere. Magnetic and electric fields are stored on a Yee-type lattice (Yee 1966). The domain is a rectangular cuboid with side length $16R_\mathrm{p}$ and computed in 3D Cartesian space with cube-sized grid cells of length $\mathrm{d}x$.

The planet is centred at $x = 0$, $y = 0$, and $z = 0$, but the domain is $x = [-12, 4]R_\mathrm{p}$, $y = [-8, 8]R_\mathrm{p}$, and $z = [-8, 8]R_\mathrm{p}$. The x-axis is anti-aligned with the undisturbed stellar wind velocity, the y-axis is the direction of the undisturbed solar wind's convection electric field, and the z-axis completes the cross-product of x and y. Throughout this study, $+E_\mathrm{sw}$ and $-E_\mathrm{sw}$ refer to the convection electric field with respect to the undisturbed solar wind, and are synonymous with $+\hat{y}$ and $-\hat{y}$, respectively. The solar wind is injected from the $+x$ wall of the domain with an initial velocity, temperature, density, and the interplanetary magnetic field (IMF). Every macroparticle that is injected into the simulation is given a particle ID, which enables seamless differentiation between solar and planetary particles. The planetary obstacle to the magnetized solar wind flow is modelled as a superconducting sphere, and ions outflowing from the ionosphere are emitted from the planet at a specified emission radius.

The upward flux of planetary ions is prescribed by a global emission rate (E_m), also known as the outflow rate, and planetary ions are produced around the dayside of the planet as a function of the cosine of the solar zenith angle. On the nightside of the planet, emission is constant at 10 per cent of the dayside emission. The outflowing population is different from the escaping population, as most outflowing ions end up recirculating back to the planet. Ions that do not recirculate back to the planet and that exit the simulation domain can be safely considered to have escaped. This escaping population is used to quantify the escape rate Q_m of each species m in ions per second, while the outflow rate at an altitude of 300 km is prescribed. The code is open source and can be found at github.com/fmihpc/rhybrid. Additional examples of RHYBRID and its algorithm can be found in the following references: Jarvinen et al. (2010, 2018, 2020), Jarvinen, Kallio & Pulkkinen (2022), and Kallio & Janhunen (2003).

2.2 Simulation parameters

We run five simulations with differently sized planets ranging from Mars to super-Earth ($R_\mathrm{p} =$ [3390 km, 5390 km, 6371 km, 7390 km, 9390 km]). However, it is impractical to vary the radius without also changing other simulation parameters (e.g. planet mass, ion emission height, simulation domain, and the ratio of grid resolution to planetary radius). The following describes every variable that is adjusted to accommodate a change in radius.

The domain is constant in units of planetary radii ($16R_\mathrm{p} \times 16R_\mathrm{p} \times 16R_\mathrm{p}$). The grid resolution is set so that across simulations the cell size is a constant fraction (6.45 per cent) of the planetary radius by setting $\mathrm{d}x = 16R_\mathrm{P}/248$. The time-step is set to $\mathrm{d}t = \mathrm{d}x/(16\,000\ \mathrm{km\,s^{-1}})$ so that the maximum velocity allowed by the Courant–Friedrichs–Lewy condition (Lewey, Friedrichs & Courant 1928) is well above the speeds reached in the simulation ($\boldsymbol{v}_\mathrm{max} = 16\,000\ \mathrm{km\,s^{-1}}$). $\boldsymbol{v}_\mathrm{max}$ is set such that it is greater than all wave speeds in the simulation (e.g. whistler waves and Alfvén waves). This large upper limit enables future studies to introduce an intrinsic planetary magnetic field without changing the time-step for a one-to-one comparison with the unmagnetized case. The resistivity of the grid, which allows the diffusion of the magnetic field above $R_\mathrm{p} + 200$ km, is $\eta_\mathrm{a} = \eta_\mathrm{c}\mu_0 \mathrm{d}x^2/\mathrm{d}t$, where μ_0 is the vacuum magnetic permeability and $\eta_\mathrm{c} = U_\mathrm{sw}\mathrm{d}t/(R_m \mathrm{d}x)$. U_sw is the solar wind bulk velocity and the magnetic Reynold's number is set to 0.25. The only diffusion implemented in the RHYBRID model is the resistive electric field term ($\eta_\mathrm{a} J$) in Faraday's law (see Jarvinen et al. 2018).

Each planet is given the density of Earth ($\rho_\mathrm{E} = 5515\ \mathrm{kg\,m^{-3}}$), and the planet's mass is computed as $M_\mathrm{p} = \rho_\mathrm{E}(4/3)\pi R_\mathrm{p}^3$. The radius where the electron velocity is forced to $\boldsymbol{v}_\mathrm{e} = 0$ and where ions are also removed from the simulation is $R_\mathrm{p} + 100$ km. The radius of the superconducting sphere is set to $R_\mathrm{p} + 200$ km, and planetary ions are emitted from $R_\mathrm{p} + 300$ km.

Measured escape rates are a lower bound for ion outflow rates; thus, a reference set of ion emission rates is defined for the Earth-sized planet based on what is analytically computed to be escaping today, $E_\mathrm{ref} = [8 \times 10^{25}\ \mathrm{H^+\,s^{-1}}, 2 \times 10^{25}\ \mathrm{O^+\,s^{-1}}]$ (Gunell et al. 2018). These reference rates are then scaled for each planet so that $E_\mathrm{p} = E_\mathrm{ref}(R_\mathrm{p}/R_\mathrm{E})^2$, ensuring that the ion emission per unit surface area remains constant.

The solar wind is initialized with $v = -400$ km s^{-1} $\hat{x}$, magnetic field $B = -5$ nT $\hat{z}$, proton density $n = 5$ cm^{-3}, temperature $T = 100\,000$ K, and 50 macroparticles per cell (mpc). Planetary O^+ and H^+ ions are injected upwards with velocity vectors normal to the planetary surface, average temperatures of 1200 K, and have 10 and 6 mpc, respectively. As we vary the planet's radius, the magnitude of the convection electric field remains roughly constant across the simulations.

Our previous study computed the net mass flux curve for an Earth-sized planet as a function of the ion outflow rate (Hinton, Brain & Schnepf 2024). In order to compare to these results, we vary the ion outflow rate for the Mars-sized planet and compute its net mass flux curve as well. We run five additional simulations for the Mars-sized planet ($E_m = [0.1E_{3390}, 0.5E_{3390}, 2E_{3390}, 5E_{3390}, 10E_{3390}]$), varying its ion outflow rate in the same way as Hinton et al. (2024) varied demagnetized Earth's ion outflow rates.

2.3 Rate extraction

The escape rate is calculated by subtracting the impact rate to the inner boundary from the injection rate for each planetary ion species. This assumes that planetary ions that do not return to the planet go on to escape the simulation domain. The solar deposition rate is the impact rate of solar hydrogen on to the inner boundary. Planetary particles are considered recirculated, and solar particles deposited, when they reach the inner boundary of $R_p + 100$ km. This altitude was selected because it is deep within the collisional atmosphere of each planet. Long before an ion reaches this altitude, it should have interacted with the planet's collisional atmosphere and either thermalized or back-scattered (Jolitz et al. 2017). Thus, the deposition rates reported in this study can be used as a direct input for models that include collisions and physical chemistry.

Each simulation is run on the University of Colorado's Alpine supercomputer. After initialization, the escape and deposition time series data eventually reach steady-state equilibrium, with some oscillatory behaviour still present. To capture this, we fit the last 10 per cent of each time series with a normal distribution and report the mean and standard deviation as our result (e.g. Figs 2 and 3 and Table 1).

3 RESULTS

In Section 3.1, we discuss the morphological changes in the heavy ion plume as R_p is increased. In Section 3.2, we discuss the escape and recirculation of H^+ and O^+ as R_p is varied. We also analyse the relevance of escape velocity to these rates. In Section 3.3, we analyse the solar wind deposition. In Section 3.4, we conduct the net mass flux analysis. Finally, in Section 3.5, we propose an end-to-end hypothesis to explain why heavy ions escape in a plume in the $+E_{sw}$ hemisphere, whereas light ions escape in a spatially confined flow out of the $-E_{sw}$ hemisphere.

3.1 Heavy ion plume as radius is varied

Spacecraft observations (Dong et al. 2015) and hybrid modelling (Jarvinen et al. 2010, 2018) are conclusive in that singly ionized oxygen atoms escape Mars in the form of a large plume in the $+E_{sw}$ hemisphere. Our results (shown in bottom row of Fig. 1) also indicate that O^+ escapes the induced magnetospheres of differently sized terrestrial planets via a similar plume.

For each planet, most of the planetary ions are produced at the sub-solar point. Along the ecliptic plane, the induced magnetic field points in the direction of the IMF ($\hat{B}_{ind} = -\hat{z}$). When an oxygen ion is injected from the sub-solar point, its velocity vector points away from the planet ($\hat{v} \approx +\hat{x}$). It immediately accelerates under the magnetic force ($\boldsymbol{F}_M = q\boldsymbol{v} \times \boldsymbol{B}$) and gyrates in the $+\hat{y}$ direction, which is towards the $+E_{sw}$ hemisphere.

The ion is also accelerated by the convection electric field ($\boldsymbol{F}_E = q\boldsymbol{E}$), thereby further increasing its gyroradius (r_g) along its trajectory. An oxygen ion moving at the bulk velocity of the solar wind of 400 km s^{-1} has a gyroradius of 11 400 km, or $3.5R_{Mars}$. This gyroradius determines the spatial extent of the ion plume in $+\hat{y}$ direction ($2r_g$ beyond the radius of the planet). The convection electric field and induced magnetic field are perpendicular, causing the plasma to drift with velocity

$$\boldsymbol{v}_d = \frac{\boldsymbol{E} \times \boldsymbol{B}}{B^2}. \quad (3)$$

The ion undergoes $\boldsymbol{E} \times \boldsymbol{B}$ drift as it escapes down the magnetotail (Jarvinen et al. 2010; Jarvinen & Kallio 2014). This illustrates how, for a Mars-sized planet, the ion plume can easily extend beyond the planet.

However, the gyroradius of the planetary ions does not change significantly as the radius is increased. As the R_p is increased, the planetary radius to gyroradius ratio is also increased, decreasing the relative size of the plume with respect to the planet. This effect is shown in Fig. 1 across the bottom row, which is a visualization of the RHYBRID simulation in the *xy* plane (the Mars-sized planet shown in red). A large portion of the plume that escapes from the Mars-sized planet is physically intercepted as the planet gets larger. As a result, the escape fraction of O^+ decreases as the radius of the planet increases, as shown in Fig. 2.

3.2 Planetary ion escape and recirculation

As R_p is increased, the absolute number of planetary ions emitted is also increased such that the emission per unit surface area is constant. Computed escape and deposition rates with 1σ uncertainties, as well as fractional rates, are reported in Table 1. Most injected ions do not escape, and instead return to the planet, i.e. recirculation. We define the recirculation fraction to be $R_m = 1 - Q_m/E_m$, which is the fraction of emitted particles of species m that end up recirculating back to the ionosphere. The absolute recirculation rates in units of *particles per second* can be found by multiplying $R_m * E_m$. Escape fractions for planetary ions are also plotted in Fig. 2.

It is shown that a consistent fraction of produced H^+ escapes from the planet (15.5 ± 1.0 per cent) as the radius is varied. This makes sense given that the morphology of the H^+ ion flow changes comparatively little as the radius of the planet is nearly tripled (see top row of Fig. 1). In order to sustain a constant escape fraction, the absolute escape rate of H^+ increases with each increase in R_p.

Unlike H^+, the absolute escape rate of O^+ is fairly constant for each simulation (see Table 1). Therefore, the fraction of produced O^+ that escapes must decrease with increasing R_p because emission rates are increasing. Mechanistically, this is in part because a larger planet presents a more significant obstacle to the heavy ion plume causing recirculation to increase as R_p increases. However, we propose an additional mechanism in Section 3.5 that can increase recirculation, which is the creation of radially inward pointing electric field vectors near the sub-solar point as R_p is increased. The slope and y intercept for the linear best-fitting function to O^+ fractional escape are $m = -3.5 \times 10^{-5}$ km^{-1} and $y = 0.39$.

The consistency of the H^+ escape fraction shows that v_{esc} is not a controlling parameter in non-thermal escape. We assume constant

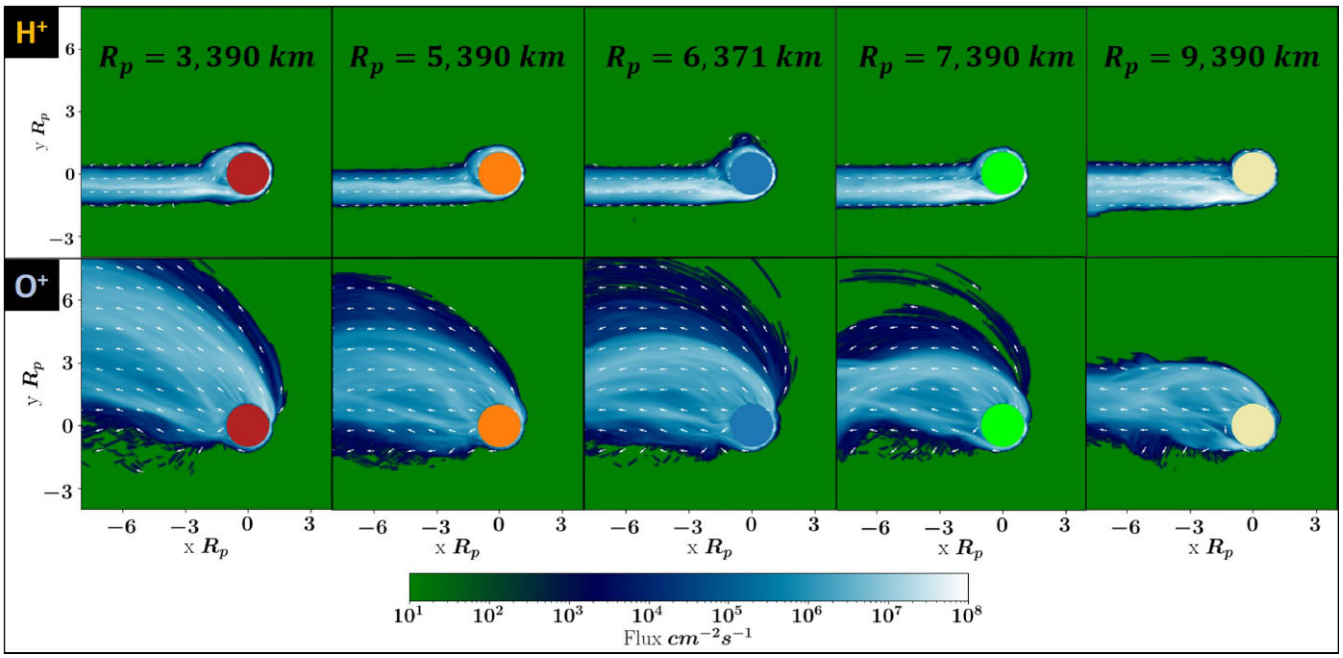

Figure 1. The five columns show simulations in the *xy* plane for the five different planetary radii simulated. The top row shows the flux of H^+ and the bottom row shows the flux of O^+. Axes are in units of planetary radius, and the convection electric field in the undisturbed solar wind points in the $+y$ direction. The colours of each planet correspond to marker colours used in Fig. 4. The H^+ escape morphology has only minor changes in units of planetary radius, whereas the O^+ plume becomes smaller as R_p is increased.

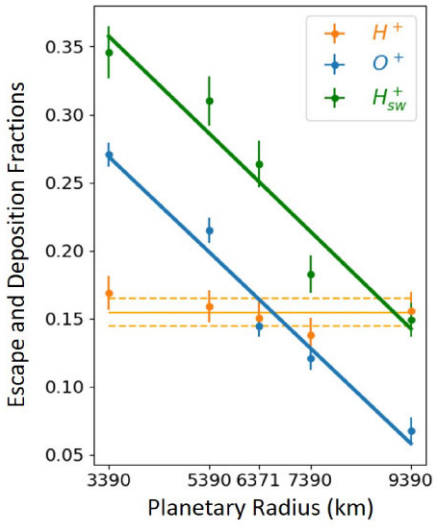

Figure 2. The escape fractions of H^+ and O^+ are shown by orange and blue circles, respectively, and the solar deposition fraction is shown by green circles. Error bars represent 1σ standard deviations on equilibrated time series data. The solid orange line and the dashed orange line are the mean and standard deviation of the computed H^+ escape fractions. The solid blue and green lines are linear best fits to computed O^+ escape fractions and the solar deposition fractions, respectively.

planetary density, which yields $v_{esc} \propto R_p$. Thus, the escape velocity changes by a factor of 2.8 from $R_p = 3390$ km to $R_p = 9390$ km; yet, the H^+ escape fractions of the two planets are statistically indistinguishable.

A short calculation elucidates this result: each planet's induced magnetic field has a magnitude of 10 nT near the bow shock, and

Table 1. Number of escaping planetary hydrogen (Q_{H^+}) and oxygen (Q_{O^+}) ions, deposition of solar hydrogen (D_{H^+}), net proton flux ($\Delta N = D_{H^+} - 16Q_{O^+} - Q_{H^+}$), the percentage of produced hydrogen and oxygen that escape (Q_m/E_m), and the percentage of solar wind from a planet-sized cross-section that deposits into the atmosphere (D_{H^+}/N_{max}).

R_p (km)	Q_{H^+} ($\times 10^{25}$ s^{-1})	Q_{O^+} ($\times 10^{25}$ s^{-1})	D_{H^+} ($\times 10^{25}$ s^{-1})	ΔN ($\times 10^{25}$ protons s^{-1})
3390	0.38 ± 0.03	0.15 ± 0.01	2.5 ± 0.1	-0.3 ± 0.2
5390	0.91 ± 0.07	0.31 ± 0.01	5.7 ± 0.3	-0.2 ± 0.4
6371	1.2 ± 0.1	0.29 ± 0.02	6.7 ± 0.4	0.9 ± 0.5
7390	1.5 ± 0.1	0.32 ± 0.02	6.3 ± 0.5	-0.4 ± 0.6
9390	2.7 ± 0.2	0.29 ± 0.04	8.3 ± 0.7	0.8 ± 1.0
R_p (km)	Q_{H^+}/E_{H^+} (per cent)	Q_{O^+}/E_{O^+} (per cent)	D_{H^+}/N_{max} (per cent)	
3390	17 ± 1	27 ± 1	35 ± 2	
5390	16 ± 1	22 ± 1	31 ± 2	
6371	15 ± 1	15 ± 1	26 ± 2	
7390	14 ± 1	12 ± 1	18 ± 1	
9390	16 ± 1	7 ± 1	15 ± 1	

increases in magnitude towards the planet. Therefore, consider 10 nT to be the lower limit of the induced magnetic field intensity at 300 km where planetary ions are injected into the induced magnetosphere. In this scenario, the force of gravity and the magnetic force are balanced ($|F_M| \approx |F_g|$) when a proton has speeds of 0.005 and 0.015 km s^{-1} for $R_p = 3390$ km and $R_p = 9390$ km, respectively.

These speeds are much lower than the typical thermal velocity at that altitude (Bilitza 2001): protons injected at 1200 K have a thermal velocity $v_{th} = (k_b T/m)^{1/2}$ of $\sim$3 km s^{-1}. This yields $|F_M|/|F_g|$ of 650 and 211, respectively. As the ions are accelerated by the convection electric field, the ratio $|F_M|/|F_g|$ quickly becomes $>10^3$. In the context of the changing O^+ escape fraction, these

results indicate that non-thermal escape is primarily controlled by the Lorentz force and the system geometry (e.g. morphology of the induced magnetosphere).

3.3 Solar wind deposition

The absolute deposition rate of solar hydrogen increases from 2.5×10^{25} to 8.3×10^{25} s^{-1} for $R_p = 3390$ km and $R_p = 9390$ km, respectively. However, the fractional deposition rate decreases from 35 per cent to 15 per cent, respectively. The fractional deposition rate is computed as the absolute rate D divided by N_{max}, which is the number of undisturbed solar wind ions that travel through a planet-sized cross-section per second,

$$N_{max} = n_{sw} v_{sw} (\pi R_p^2), \tag{4}$$

where n_{sw} is the density of the wind (5 cm^{-3}) and v_{sw} is the speed of the solar wind (400 km s^{-1}). The fractional deposition rate can also be thought of as the planet's solar proton albedo. Some fraction of oncoming protons are redirected around the planet, while the rest are effectively absorbed by the planet.

The decrease in proton albedo can be explained by solar ions experiencing deflection at greater distances from the planet. In each simulation, the bow shock of the induced magnetic field forms at $r_{bs} = (1.55 \pm 0.05) R_p$. Thus, as R_p increases, so do both the bow shock altitude and the bow shock's ability to slow and redirect solar wind ions. The result is a decrease in the fractional deposition rate, which also causes the absolute deposition to deviate significantly from a quadratic R_p^2 dependence. The slope and y intercept for the linear best-fitting function to the solar proton albedo are $m = -3.6 \times 10^{-5}$ km^{-1} and $y = 0.48$. These approximations are only valid for the domain and assumptions used in this study.

3.4 Net mass flux analysis

In order to compare the escaping mass with the mass that is being deposited, the escaping ions are quantified in terms of their total proton count ($Q_{proton} = Q_{H^+} + 16Q_{O^+}$). This enables a one-to-one comparison as the deposited mass is simply solar wind protons that impact the planet's collisional atmosphere. We find that for each radius tested in this study, the 1σ error bars of escaping and depositing mass overlap each other, as shown in Fig. 3. This suggests that the escaping mass is roughly equal to the deposited mass for the outflow rates simulated.

This happens to be a coincidence regarding the set of ion outflow rates simulated. Hinton et al. (2024) found that for unmagnetized planets in constant solar wind conditions, there exists a critical ion emission rate E_{crit} at which the depositing mass perfectly cancels out the escaping mass. The Earth reference set happens to be very close to this critical value ($E_{ref} \approx E_{crit}$). In this study, we scale this reference set for each of the planetary radii tested and find that the escape appears to nearly equal the deposition for each primary run. What we have found is that

$$E_{crit} \propto R_p^2. \tag{5}$$

This relationship is illustrated in Fig. 4, which shows that the ΔN of the five primary runs of this study falls on or very near the horizontal black line. This line represents a net atmospheric mass flux of zero. We also plot the Hinton et al. (2024) result (blue line) to show the net mass flux of demagnetized Earth ($R_p = 6371$ km) as a function of the total ion outflow rate. The upper limit on the net mass flux profile, set by the cross-sectional area of the intercepting planet, will certainly be lower for smaller planets. To investigate whether the rest of the net mass flux curve might have a clear dependence

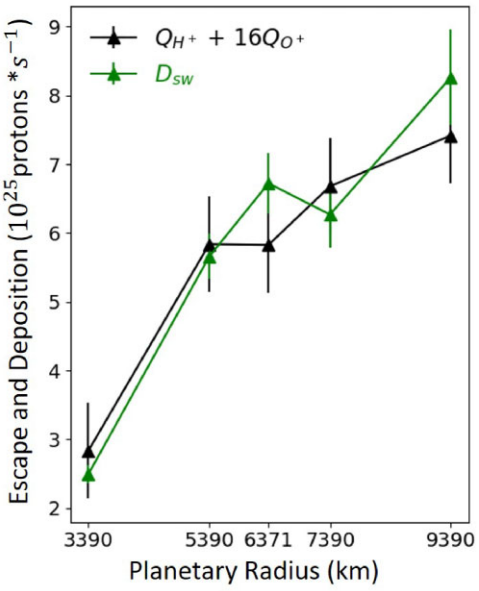

Figure 3. The green triangles are computed solar deposition rates (D). The black triangles are the computed total proton escape rates (Q). For each of the five simulations, the 1σ error bars of escape and deposition overlap.

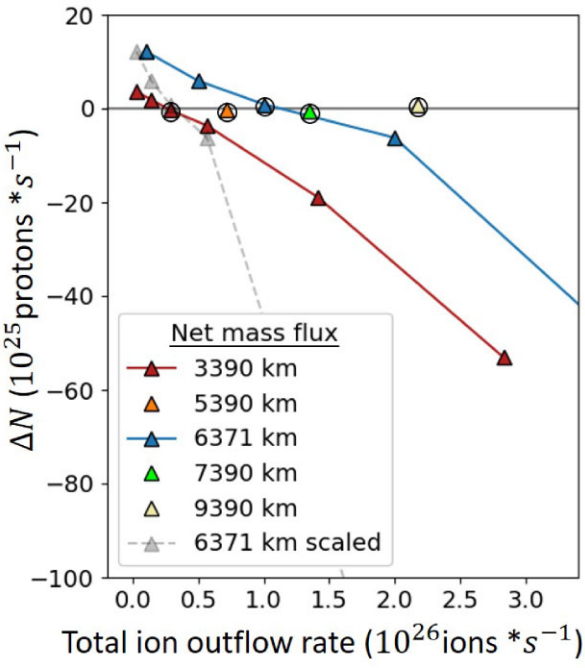

Figure 4. The y-axis is the change in proton number of the upper atmosphere of the planet ($\Delta N = D_{sw} - [Q_{H^+} + 16Q_{O^+}]$). The x-axis is the total ion outflow rate ($E_{H^+} + E_{O^+}$). The five main simulations of this study are the circled coloured triangles that intersect with the $\Delta N = 0$ line. The dashed grey line with grey triangles is demagnetized Earth's net mass flux line (blue), with x values shifted by R_{Mars}/R_{Earth} for comparison.

on R_p^2, we vary the ion outflow rates of the Mars-sized planet and compute its net mass flux curve (depicted in Fig. 4 by the red line).

We then scale demagnetized Earth's net mass flux profile down to the Mars-sized planet's by multiplying each ΔN value by $(3390/6371)^2$. This is shown by the grey dashed line in Fig. 4. We find that only the critical emission rate is well matched, and the rest

of the net mass flux curve quickly deviates from what is computed for R_{3390}. Likewise, the net mass flux curve for demagnetized Earth cannot simply be shifted in the $-x$ direction to match the Mars-sized planet's net mass flux curve.

3.5 Solar wind kinetics leading to differential ion escape trajectories

In Section 3.1, we described the formation of the heavy ion plume, which primarily escapes out of the $+E_{sw}$ hemisphere. Jarvinen et al. (2010) find that light ions behave as a magnetized fluid and follow lines in the $\boldsymbol{E} \times \boldsymbol{B}$ vector field. They note that $\boldsymbol{E} \times \boldsymbol{B}$ streamlines concentrate in the H^+ wake in the $-E_{sw}$ hemisphere, and that this is due to asymmetric deflections of the solar wind (Saunders & Russell 1986; Brecht 1990; Zhang et al. 2010). We agree with this analysis and expand on it in light of the present findings.

There is a subtle morphological trend in the escape flows of this study that can be observed in Fig. 1. For $R_p = 3390$ km, the vast majority of escaping O^+ exits over the $+E_{sw}$ pole. However, for $R_p = 9390$ km, an appreciable amount of the O^+ flux passes over the $-E_{sw}$ pole. As the radius is increased, the flow of planetary ions beginning at the sub-solar point and passing over the $+E_{sw}$ pole generally decreases, while the flow over the $-E_{sw}$ pole increases. This effect is also observed in planetary H^+ ions.

We hypothesize that this effect is due to gyromotion of the solar wind. As the solar wind encounters the increased magnetic field intensity environment of the induced magnetosphere, it will begin to bulk gyrate towards the $-\hat{E}_{sw}$ hemisphere. As R_p increases, the altitude of the bow shock also increases. This entails that solar protons will spend a greater amount of time in the induced magnetosphere on the dayside of the planet, which increases the asymmetric deflection due to gyromotion.

As the solar wind turns towards $-\hat{E}_{sw}$ (defined with respect to the undisturbed wind), the local convection electric field structure in the sub-solar region begins to point radially inwards to reflect this change in trajectory. As a result, the local $\boldsymbol{E} \times \boldsymbol{B}$ vectors point in the direction of the travelling solar wind, which remains generally true across the simulation domain.

Ions with a small gyroradius (i.e. H^+) may gyrate within the region and follow $\boldsymbol{E} \times \boldsymbol{B}$ drift vectors towards the $-\hat{E}_{sw}$ hemisphere, whereas ions with a larger gyroradius (i.e. O^+) exit this localized region and separate from the planet where the drift vectors instead point along the magnetosheath. As the scale size (r_c) of the region of inward pointing $\boldsymbol{E}$ field gets larger, its ability to contain particle gyromotion increases. The important quantity is the ratio between the size of the region and the gyroradius of outflowing ions ($r_c/r_{g,i}$). This hypothesis, which can explain the different light and heavy ion trajectories, is illustrated in Fig. 5.

The area of inward pointing electric field vectors in the sub-solar region first becomes noticeable at $R_p = 5390$ km and then grows larger as R_p is increased. Fig. A1 shows this region for each of the five planetary radii tested. This corresponds to what is seen in Fig. 1, where the flux of planetary H^+ over the $+E_{sw}$ and $-E_{sw}$ poles is comparable for $R_p = 3390$ km and then gradually shifts to the $-E_{sw}$ pole as the planetary radius is increased. The size of the region with inward pointing electric field vectors appears to be $\propto R_p$. This suggests that as R_p is increased, more ions would gyrate within this region and drift out of the $-E_{sw}$ hemisphere, as is observed in both H^+ and O^+ in Fig. 1. This effect likely contributes to the increased recirculation of O^+ as R_p is increased.

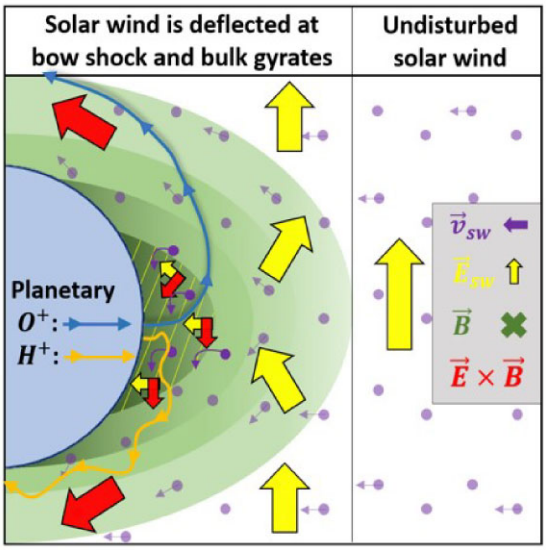

Figure 5. The undisturbed solar wind is shown on the right. On the left, the solar wind flow is slowed at the bow shock and deflected to either side of the planet due to pressure gradients (Russell 2000). As it enters the induced magnetosphere, it begins gyromotion, causing the convection electric field to point towards the planet. This creates $\boldsymbol{E} \times \boldsymbol{B}$ vectors pointing in the undisturbed $-\hat{E}_{sw}$ direction. H^+ can gyrate within this region and drift to $-E_{sw}$, while O^+ typically gyrates out of this region towards the $+E_{sw}$ hemisphere.

4 DISCUSSION

These findings suggest that, all else being equal, smaller planets will have a more difficult time retaining heavy ions than larger planets. This may be important for guiding future exoplanet studies (Léger et al. 2011), as Earth- and super-Earth-sized planets are more capable of maintaining their heavy ion supplies. However, smaller planets also interact more closely with the solar wind, which allows a greater fraction of the solar wind to penetrate inwards and precipitate.

For Mars-sized planets, these two effects work to increase their inventories of light ions and decrease their inventories of heavy ions. Thus, as the planetary radius is increased, the heavy ion to light ion ratio may also increase. This suggests that planets of different sizes may be predisposed to different redox rates (Schaefer & Fegley 2017), which can effect the evolution of life (Koyama et al. 2021). It is important to note that the physics of depositing particles has been simplified in this study and does not include charge exchange (Halekas et al. 2015), which can lead to penetrating neutral atoms (Barabash et al. 1995; Kallio, Luhmann & Barabash 1997; Holmström, Barabash & Kallio 2002). Depositing particles can either thermalize or back-scatter (Jolitz et al. 2017). During thermalization, it is possible to produce proton aurora (Chaffin et al. 2022), which can also be used as validation for hybrid model results (Kallio & Janhunen 2001).

Chin et al. (2024) recently conducted a similar study that used BATSRUS (Powell et al. 1999), a non-kinetic magnetohydrodynamic model, under Venusian atmospheric assumptions (Moroz 1981), to quantify escape as a function of R_p. The study only considered heavy ion escape, but covered a larger range of radii ($R_p = 3026$–$13\,617$ km). They find that the absolute escape of O^+ generally decreases with planetary radius, whereas we find that the absolute escape of oxygen remains fairly stable as radius is increased.

However, their atmospheric assumptions do not lead to a constant ionospheric outflow per unit surface area as the planetary radius is

varied; thus, these two results are not directly comparable in this way. Moreover, exospheric ion production was neglected in this study and its role, especially at smaller planets, should be analysed in future studies. None the less, applying our results to Chin et al. (2024) suggests that the trend they observe of generally decreasing heavy ion escape with increasing R_p would be even more exaggerated if they included ion kinetics due to increased recirculation.

5 CONCLUSIONS

The main conclusions of this study are as follows:

(i) Regarding the ionospheric outflow of H^+, we find that the fraction that escapes as the planetary radius is varied remains roughly constant at 15.5 ± 1.0 per cent, with most of the ionospheric outflow recirculating back towards the planet.

(ii) As the radius of the planet is increased, more of the heavy ion plume is intercepted by the planet, causing the escape fraction of O^+ to decrease.

(iii) Non-thermal escape is primarily controlled by the Lorentz force and the system geometry, not by the kinetic energy of produced ions.

(iv) The solar deposition fraction decreases as R_p is increased due to increase in the bow shock distance.

(v) The ion emission rate at which escaping and deposited masses are in equilibrium (E_{crit}) is proportional to R_p^2. This means that larger planets require greater emission rates in order to have net mass escape.

We observe that as R_p increases, both ion escape flows are amplified in the $-E_{sw}$ hemisphere. We provide a hypothesis to explain this, which is that the solar wind's kinetic response to the induced planetary magnetic field is responsible for the differential escape trajectories and has a positive dependence on R_p. Testing this hypothesis is the immediate focus of our future work.

Lastly, this study shows how the morphology of escaping ion plumes changes as the planetary radius is changed. To zeroth order, the H^+ escape morphology, i.e. the spatial dimensions of the plume, remains constant in units of planetary radii, whereas the relative size of the O^+ plume decreases. This study suggests that differences in the heavy ion plume are attributable to the ratio between the gyroradius and the planetary radius. These findings, combined with the escape rate as a function of planetary radius, help contribute to a general understanding of ion escape and can be applied to differently sized exoplanets.

ACKNOWLEDGEMENTS

This work utilized the Alpine high-performance computing resource at the University of Colorado Boulder. Alpine is jointly funded by the University of Colorado Boulder, the University of Colorado Anschutz, Colorado State University, and the National Science Foundation (award 2201538). Simulations were performed using the RHYBRID code distributed under the open source GPL v3 license by the Finnish Meteorological Institute (github.com/fmihpc/rhybrid). Funding for this work was provided by the National Solar Observatory George Ellery Hale Fellowship and by the Retention of Habitable Atmospheres in Planetary Systems grant 80NSSC23K1358 awarded by the National Aeronautics and Space Administration's Interdisciplinary Consortia for Astrobiology Research programme. RJ received funding from the European Research Council (Grant agreement No. 101124960).

DATA AVAILABILITY

The data used in this study can be found by referring to Table 1. The model that generated these data, RHYBRID, is open source and can be found at https://github.com/fmihpc/rhybrid, and is run with simulation parameters described in this study. The simulation code version used in this study is archived (doi: 10.5281/zenodo.10836240).

REFERENCES

Barabash S., Lundin R., Zarnowiecki T., Grzedzielski S., 1995, Adv. Space Res., 16, 81
Bilitza D., 2001, Radio Sci., 36, 261
Brain D. A., Bagenal F., Ma Y.-J., Nilsson H., Stenberg Wieser G., 2016, J. Geophys. Res. Planets, 121, 2364
Brecht S. H., 1990, Geophys. Res. Lett., 17, 1243
Carr M. H., Waenke H., 1992, Icarus, 98, 61
Chaffin M. S. et al., 2022, Geophys. Res. Lett., 49, e99881
Chin L., Dong C., Lingam M., 2024, ApJ, 963, L20
di Achille G., Hynek B. M., 2010, Nat. Geosci., 3, 459
Dong Y. et al., 2015, Geophys. Res. Lett., 42, 8942
Dubinin E., Fraenz M., Woch J., Barabash S., Lundin R., 2009, Geophys. Res. Lett., 36, L08108
Egan H. et al., 2018, J. Geophys. Res. Space Phys., 123, 3714
Ergun R. E., Andersson L., Peterson W. K., Brain D., Delory G. T., Mitchell D. L., Lin R. P., Yau A. W., 2006, Geophys. Res. Lett., 33, L14103
Fang X., Liemohn M. W., Nagy A. F., Ma Y., De Zeeuw D. L., Kozyra J. U., Zurbuchen T. H., 2008, J. Geophys. Res. Space Phys., 113, A02210
Fang X., Liemohn M. W., Nagy A. F., Luhmann J. G., Ma Y., 2010, J. Geophys. Res. Space Phys., 115, A04308
Gunell H., Maggiolo R., Nilsson H., Stenberg Wieser G., Slapak R., Lindkvist J., Hamrin M., De Keyser J., 2018, A&A, 614, L3
Haider S. A., Mahajan K. K., Kallio E., 2011, Rev. Geophys., 49, RG4001
Halekas J. S. et al., 2015, Geophys. Res. Lett., 42, 8901
Hinton P. C., Brain D. A., Schnepf N. S., Jarvinen R., Cessna J., Bagenal F., 2024, Research Square, https://doi.org/10.21203/rs.3.rs-4255286/v1
Holmström M., Barabash S., Kallio E., 2002, J. Geophys. Res. Space Phys., 107, 1277
Jakosky B. M., 2022, Phys. Today, 75, 62
Jarvinen R., Kallio E., 2014, J. Geophys. Res. Planets, 119, 219
Jarvinen R., Kallio E., Dyadechkin S., Janhunen P., Sillanpää I., 2010, Geophys. Res. Lett., 37, L16201
Jarvinen R., Brain D. A., Luhmann J. G., 2016, Planet. Space Sci., 127, 1
Jarvinen R., Brain D. A., Modolo R., Fedorov A., Holmström M., 2018, J. Geophys. Res. Space Phys., 123, 1678
Jarvinen R., Alho M., Kallio E., Pulkkinen T. I., 2020, Geophys. Res. Lett., 47, e87462
Jarvinen R., Kallio E., Pulkkinen T. I., 2022, J. Geophys. Res. Space Phys., 127, e30078
Jolitz R. D. et al., 2017, J. Geophys. Res. Space Phys., 122, 5653
Kallio E., Janhunen P., 2001, J. Geophys. Res., 106, 5617
Kallio E., Janhunen P., 2003, Ann. Geophys., 21, 2133
Kallio E., Luhmann J. G., Barabash S., 1997, J. Geophys. Res., 102, 22183
Koyama S., Terada N., Nakagawa H., Kuroda T., Sekine Y., 2021, ApJ, 912, 135
Léger A., Fontecave M., Labeyrie A., Samuel B., Demangeon O., Valencia D., 2011, Astrobiology, 11, 335
Lewey H., Friedrichs K., Courant R., 1928, Math. Ann., 100, 32
Lillis R. J. et al., 2015, Space Sci. Rev., 195, 357
Moroz V. I., 1981, Space Sci. Rev., 29, 3
Powell K. G., Roe P. L., Linde T. J., Gombosi T. I., De Zeeuw D. L., 1999, J. Comput. Phys., 154, 284
Richards P. G., Voglozin D., 2011, J. Geophys. Res. Space Phys., 116, A08307
Russell C. T., 2000, IEEE Trans. Plasma Sci., 28, 1818
Saunders M. A., Russell C. T., 1986, J. Geophys. Res., 91, 5589
Schaefer L., Fegley B., Jr, 2017, ApJ, 843, 120

Slavin J. A., Holzer R. E., 1981, J. Geophys. Res., 86, 11401
Sun W., Ma Y., Russell C. T., Luhmann J., Nagy A., Brain D., 2023, J. Geophys. Res. Space Phys., 128, e2023JA031301
Valencia D., O'Connell R. J., Sasselov D., 2006, Icarus, 181, 545
Wang X.-D., Fatemi S., Nilsson H., Futaana Y., Holmström M., Barabash S., 2023, MNRAS, 521, 3597
Xu Q., Xu X., Zuo P., Futaana Y., Chang Q., Gu H., 2023, Geophys. Res. Lett., 50, e2022GL102401
Yee K., 1966, IEEE Trans. Antennas Propag., 14, 302
Zhang T. L. et al., 2010, Geophys. Res. Lett., 37, L14202

SUPPORTING INFORMATION

Supplementary data are available at *MNRAS* online.

3390.cfg
5390.cfg
7390.cfg
9390.cfg

Please note: Oxford University Press is not responsible for the content or functionality of any supporting materials supplied by the authors. Any queries (other than missing material) should be directed to the corresponding author for the article.

APPENDIX A: ELECTRIC FIELD VECTORS

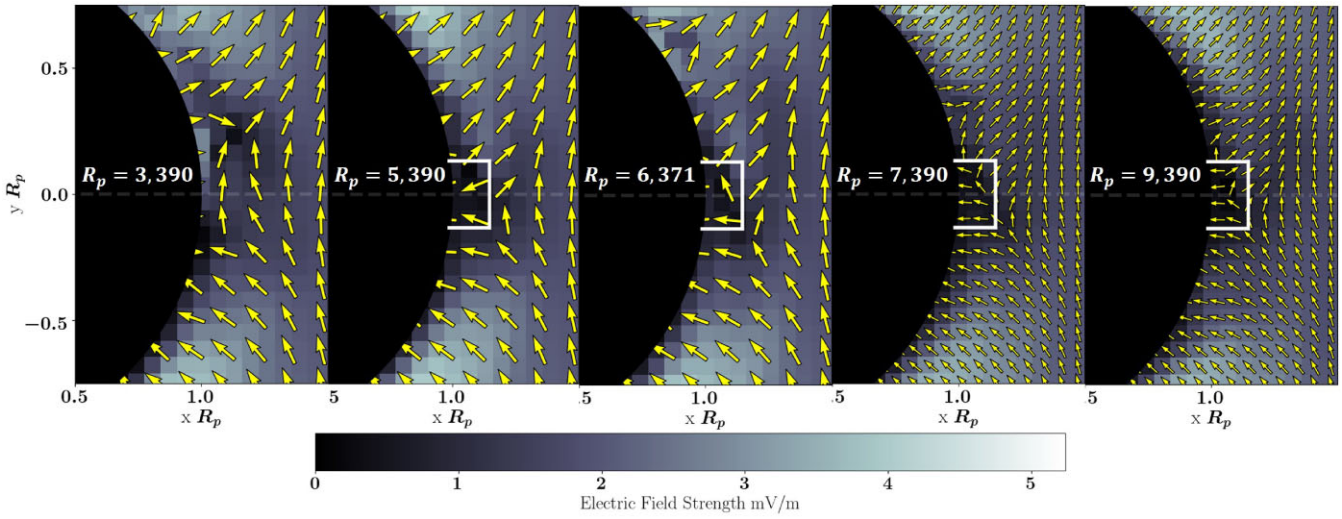

Figure A1. The $\boldsymbol{E}$ vector field for each planetary radius is shown in yellow. The electric field strength increases from dark to light. The planetary radius in units of km is displayed in white text over the black planets. The white box around the sub-solar point roughly shows where $\boldsymbol{E} \times \boldsymbol{B}$ vectors point towards the $-E_{\rm sw}$ hemisphere. Additional vector density is shown for the two largest planets to illustrate finer structure. The vector field for $R_{\rm p} = 6371$ km was used to create the illustration shown in Fig. 5.

This paper has been typeset from a TEX/LATEX file prepared by the author.